

Comparative Analysis of Potential Calibration Alternatives for a Multi-Unit LiDAR System

Yun-Jou Lin *, Radhika Ravi, Tamer Shamseldin, Magdy Elbahnasawy, Darcy Bullock, Ayman Habib
Lyles School of Civil Engineering, Purdue University, 550 Stadium Mall Dr., West Lafayette, IN 47907, USA
- (yjin, ravi22, tshamsel, melbahn, darcy, ahajib)@purdue.edu

KEY WORDS: Outdoor Calibration, Multi-Unit LiDAR System, Mounting Parameters, HDL32E, VLP16

ABSTRACT:

Nowadays, mobile mapping systems that can rapidly collect 3D spatial data geo-referenced to a global reference frame have become popular for a variety of applications such as Digital Building Model (DBM) generation, transportation corridor monitoring, telecommunications, precision agriculture, and infrastructure monitoring. To derive point clouds with high positional accuracy from an integrated system of LiDAR sensors and GNSS/INS, calibration of mounting parameters is the foremost and necessary step. This paper proposes a multi-unit LiDAR system calibration procedure that can directly estimate the mounting parameters relating the different laser scanners to the onboard GNSS/INS unit through an outdoor calibration procedure.

The proposed calibration procedure is based on the use of conjugate planar/linear features in overlapping point clouds derived from different drive-runs. In order to increase the efficiency of semi-automatic conjugate feature extraction, specifically designed calibration boards covered by highly reflective surfaces that could be easily deployed and setup within outdoor environments are used in this study. The comparative analysis as well as the performance of the potential system calibration procedures is evaluated using a multi-unit mobile LiDAR system comprised of: 1) a Velodyne HDL-32E laser scanner, 2) a Velodyne VLP-16 laser scanner, and 3) a SPAN CPT direct geo-referencing GNSS/INS unit. The comparative performance of the different calibration alternatives will be evaluated through: 1) a-posteriori variance factor of the least-squares adjustment procedure; 2) quality of fit of the adjusted point clouds to planar surfaces before and after the calibration process. Moreover, this system is going to be used for a lane width evaluation application. A comparison of on-site manually measured lane width and extracted lane width from calibrated point clouds is provided to prove that the proposed procedure can be used in high-accuracy surveying application.

1. INTRODUCTION

LiDAR scanners onboard airborne and terrestrial platforms have been established as a proven technology for the acquisition of dense point clouds with high positional accuracy. The main factors behind the widespread use of LiDAR systems include the ever-continuous improvement in GNSS/INS direct geo-referencing technology as well as enhanced performance and reduced size and cost of laser scanning units. Currently, there are commercially available LiDAR units that are capable of emitting more than a quarter million pulses per second at a cost of less than \$10k. Such availability, together with the ever-increasing range of applications – such as Digital Building Model generation, transportation corridor monitoring, telecommunications, precision agriculture, infrastructure monitoring, seamless outdoor-indoor mapping, and power line clearance (Lin et al., 2013; Williams et al., 2013; Weiss and Biber, 2011; Puente et al., 2013) – have led to the development of multi-unit mobile LiDAR systems onboard airborne and terrestrial platforms that are either manned or unmanned. However, the attainment of the full positioning potential of such systems is contingent on an accurate calibration of the mobile mapping unit as a whole. This paper proposes a multi-unit LiDAR system calibration procedure that can directly estimate the mounting parameters relating the different laser scanners to the onboard GNSS/INS unit through an outdoor calibration procedure.

The cost-effective Velodyne laser scanner, which has multi-firing laser beams and can rapidly capture a high volume of data, has been used in many mobile mapping systems and robotics applications (Schwarz, 2010; Choi, 2014; Vallet et al., 2015). Over the past few years, a great deal of research has been studied on modeling the error of Velodyne laser scanners as well as the

calibration of integrated LiDAR sensor and GNSS/INS direct geo-referencing units (Atanacio-Jiménez et al., 2011; Glennie et al., 2013). Underwood et al. (2007) calibrated the extrinsic parameters of a SICK LMS-291 and Novatel Synchronized Position Attitude Navigation (SPAN) system by minimizing the error between sensed data and a known structure (i.e., a vertical pole and relatively flat ground). He et al. (2013) used pairwise multi-type 3D geometric features (i.e., point, line, plane) to derive the extrinsic parameters between 2D LiDAR and GNSS/INS. First, the points are segmented into different features and their quality is evaluated to compute weights to be used in the minimization of normal distance between conjugate features. However, when the initial parameters are considerably inaccurate, the segments and derived weights may not be reliable. Chan et al. (2013) introduced an intrinsic parameters calibration for Velodyne HDL-32E based on static stations and also analyzed the temporal stability of range measurements which indicated an approximate warm-up time of 2000 sec for most laser beams. Glennie et al. (2016) performed a geometric calibration with stationary VLP-16 to marginally improve the accuracy of the point clouds by approximately 20%. Moreover, this paper also investigates the range accuracy of VLP-16, which is quoted to have an RMSE value between 22 to 27 mm in the factory supplied calibration certificate. But, it is observed that some of the laser beams have a worse range accuracy than the others. Although many LiDAR system calibration procedures have been developed in the past, outdoor calibration of integrated GNSS/INS and multi-unit 3D laser scanners is still an active area of research.

This paper is focusing on the potential calibration alternatives of a multi-unit LiDAR system onboard a terrestrial mobile mapping vehicle. The focus of the system calibration is to estimate the mounting parameters relating the different system components simultaneously. More specifically, the lever arm and boresight

* Corresponding author. This is useful to know for communication with the appropriate person in cases with more than one author.

angles relating the individual laser scanners and the onboard GNSS/INS unit will be derived. Moreover, this paper provides an iterative calibration procedure that can accurately estimate mounting parameters using initial approximations. The multi-unit mobile LiDAR system used for this research consists of the following components: 1) a Velodyne HDL-32E laser scanner, 2) a Velodyne VLP-16 laser scanner, and 3) a SPAN CPT direct geo-referencing GNSS/INS unit. The comparative performance of the different calibration alternatives will be evaluated through: 1) a-posteriori variance factor of the least squares adjustment procedure; 2) quality of fit of the adjusted point clouds to planar surfaces before and after the calibration process. Moreover, this mobile system is also adopted for a lane width evaluation application. A comparison of on-site manually measured lane width and extracted lane width from calibrated point clouds is provided to demonstrate the feasibility of proposed strategy.

2. SPECIFICATIONS FOR LiDAR UNITS AND NAVIGATION SYSTEM USED IN THIS RESEARCH

HDL-32E is 149.86 mm high, 85.3 mm in diameter and weighs 1 kg (plus 0.3kg for cabling). It consists of 32 radially-oriented laser rangefinders that are aligned from $+10.67^\circ$ to -30.67° . In total, the vertical Field of View (FOV) is 41.34° . A 3D Velodyne can rotate the whole unit to achieve a 360° horizontal FOV. The reliable return range is approximately from 1 m to 70 m and the point capture rate is around 700,000 points per second (Velodyne (a), 2016).

VLP-16, that has 16 radially-oriented laser rangefinders, is a lite version of HDL-32E. The vertical FOV is from -15° to $+15^\circ$ and the horizontal FOV is 360° . The effective range is from 1 m to 100 m depending on the application, and the point capture rate is around 300,000 points per second (Velodyne (b), 2016).

The navigation system adopted in this research is SPAN-CPT that combines GNSS and Inertial Measurement Unit (IMU) hardware inside a single enclosure. The GNSS position collection rate is 20 Hz and IMU measurement rate is 100 Hz. The accuracy in position can be less than 2 cm. For the attitude, the accuracy can achieve 0.008° and 0.035° in the roll/pitch and heading directions, respectively (Novatel, 2014).

3. PROPOSED CALIBRATION PROCEDURE

In this section, we propose a strategy to calibrate the mounting parameters using geometric features (e.g., planar, and linear/cylindrical features). After collecting data from several drive-runs, a 3D point cloud relative to a global reference frame will be derived through a direct geo-referencing system. Then, conjugate features are identified and extracted from the reconstructed point cloud. Finally, an iterative multi-system calibration with weight modification is proposed to derive the mounting parameters based on the minimization of normal distance between conjugate features.

3.1 Conceptual Basis of LiDAR Point Positioning

A typical directly geo-referenced LiDAR system could involve 3 coordinate systems (i.e., mapping frame, IMU body frame, and laser unit frame). A given point, I , acquired from a mobile mapping system can be reconstructed in the mapping coordinate system using Equation 1, which is graphically illustrated in Figure 1. For the laser unit frame, origin is defined at the laser beam firing point and the z-axis is along the axis of horizontal rotation of the laser unit. For a Velodyne system, each laser beam is fired at a fixed vertical angle, α , the horizontal angle, β , is

determined based on the rotation of the unit, and the range, ρ , is defined by the distance from firing point to its footprint. So, the coordinates of a 3D point relative to the Velodyne laser unit coordinate system, $r_I^{lu}(t)$, is defined by Equation 2. An IMU body frame should be considered when mobile systems are equipped with a GNSS/INS navigation unit. For mobile systems, the lever arm, r_{lu}^b , and boresight matrix, R_{lu}^b , between laser unit and body frame coordinate systems are time-independent as the laser units are fixed rigidly with respect to the IMU unit. The GNSS/INS integration provides the time-dependent position, $r_b^m(t)$, and rotation, $R_b^m(t)$, relating the mapping frame and IMU body frame coordinate systems, according to the optimized solution from all the available GNSS and inertial measurements.

$$r_I^m = r_b^m(t) + R_b^m(t) r_{lu}^b + R_b^m(t) R_{lu}^b r_I^{lu}(t) \quad (1)$$

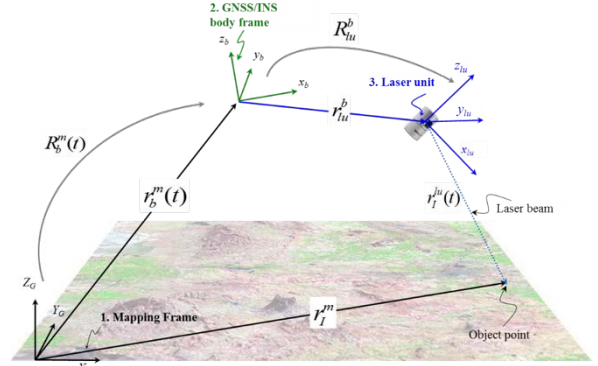


Figure 1. Illustration of point positioning of a directly geo-referenced LiDAR system

$$r_I^{lu}(t) = \begin{pmatrix} x \\ y \\ z \end{pmatrix} = \begin{pmatrix} \rho(t) \cos \beta(t) \cos \alpha(t) \\ \rho(t) \cos \beta(t) \sin \alpha(t) \\ \rho(t) \sin \beta(t) \end{pmatrix} \quad (2)$$

The mathematical formulation for computing the mapping frame coordinates of an object point for 3D point reconstruction from a multi-laser unit system is provided in Equation 3, where a reference sensor and slave sensors are considered. An illustration of such a multi-unit LiDAR system is shown in Figure 2. In Equation 3, the terms r_{lur}^b and R_{lur}^b are the lever arm and boresight matrix, respectively, relating the IMU body frame and the reference laser unit coordinate systems. The extra terms considered in Equation 3, r_{luj}^{tur} and R_{luj}^{tur} are the lever arm and boresight matrix, respectively, rigidly relating the reference sensor, lur , and the slave sensor, luj . One can introduce one or more slave sensors, each one of them rigidly related to the reference sensor by a lever arm and boresight matrix. When a point is acquired by a reference sensor, then r_{luj}^{tur} is zero and R_{luj}^{tur} is an identity matrix. In this scenario, Equation 3 will reduce to Equation 1.

$$r_I^m = r_b^m(t) + R_b^m(t) r_{lur}^b + R_b^m(t) R_{lur}^b r_{luj}^{tur} + R_b^m(t) R_{lur}^b R_{luj}^{tur} r_I^{luj}(t) \quad (3)$$

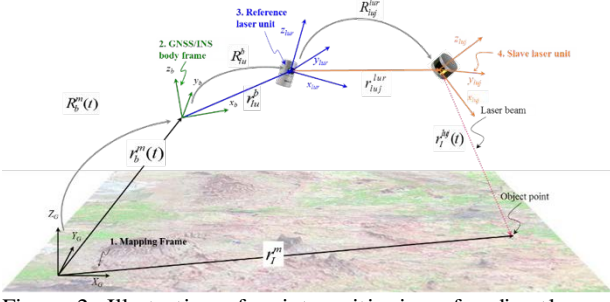


Figure 2. Illustration of point positioning of a directly geo-referenced multi-unit LiDAR system

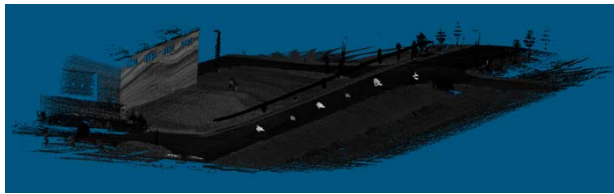
3.2 Feature Extraction

After reconstructing the point clouds from several drive-runs using the initial estimates for mounting parameters, different types of geometric features (i.e., planar, and linear/cylindrical) can be used as conjugate features for the calibration procedure. However, conjugate point pairs cannot be used since there is no accurate point-to-point correspondence, owing to the irregular distribution of LiDAR points. But, linear/cylindrical and planar features, such as building façade, ground patches, light poles, and lane markers, can be directly extracted from overlapping areas within the drive-runs. However, conjugate feature extraction from several drive-runs could be time-consuming and inefficient, especially when the initial parameters are considerably inaccurate. To facilitate automated identification of conjugate features in such cases, specifically designed calibration boards covered by highly reflective surfaces, that could be easily deployed and setup in outdoor environments, are used in this study, as shown in Figure 3 (a).

The highly reflective boards can be easily identified from intensity data as shown in Figure 3 (b). Firstly, a pre-defined threshold is set to extract the high-intensity points. To avoid the extraction of objects, other than these boards, with high-intensity points, an approximate pre-set region is set as seed points for each board. Then, a distance-based region growing technique is adopted to group the high intensity boards. Other planar features, such as ground patches, can be easily extracted by defining two diagonally opposite corners.



(a)



(b)

Figure 3. (a) Image, and (b) Intensity data of specifically designed highly reflective surfaces from a single drive-run.

3.3 Multi-Sensor System Calibration

In the proposed calibration method, conjugate features are extracted from the point clouds of different sensors and several drive-runs. The mounting parameters of each sensor are derived by minimizing the discrepancies among conjugate features in overlapping drive-runs. The ideal mathematical condition for a conjugate point pair from two overlapping drive-runs is given by Equation 4. However, for non-conjugate points along corresponding planar and linear/cylindrical features, the misclosure vector, \bar{D} , would lie along the planar surface or along the linear feature/axis of cylinder, as illustrated in Figure 4. Therefore, a modified weight matrix, P' , is introduced to eliminate the non-random component of misclosure vector, \bar{D} (Renaudin et al., 2011) (Equation 5). To derive this matrix, a local coordinate system (UVW) is established first. For linear/cylindrical features, U -axis is aligned along the line/axis of cylinder and V - and W -axes are arbitrarily chosen to satisfy the orthogonality constraint. For planar features, W -axis is aligned along the normal vector of a plane in question, and U - and V -axes are arbitrarily chosen. An illustration of the local coordinate systems for the two types of features is shown in Figure 5. Then, a rotation matrix, R_{XYZ}^{UVW} , is derived according to the components of the vectors, U , V , and W , to relate the local and mapping coordinate systems. This is discussed in more detail later. The weight matrix, P_{XYZ} , in mapping coordinate system is transformed to a weight matrix, P_{UVW} , in the local coordinate system according to the law of error propagation (Equation 6). The weight matrix, P_{UVW} , is modified by assigning a zero weight to the elements corresponding to the misclosure vector direction. More specifically, the misclosure vector can be eliminated by setting a zero weight in the corresponding direction. The misclosure direction of a linear/cylindrical feature is along the U -axis. Therefore, the modified weight matrix, P'_{UVW} , has zero weight in all the elements pertaining to the U -axis (Equation 7). Similarly, the misclosure vector direction of a planar feature is along the U - and V -axes. So, all the elements pertaining to the U - and V -axes are assigned a zero weight (Equation 8). Finally, the modified weight matrix, P'_{XYZ} , in the mapping coordinate system is derived using Equation 9. Finally, the condition given by Equation 4 can be modified to account for non-conjugate points along corresponding features within overlapping drive-runs by applying the obtained modified weight matrix, P'_{XYZ} .

$$r_i^m(\text{drive-run 1}) - r_i^m(\text{drive-run 2}) = 0 \quad (4)$$

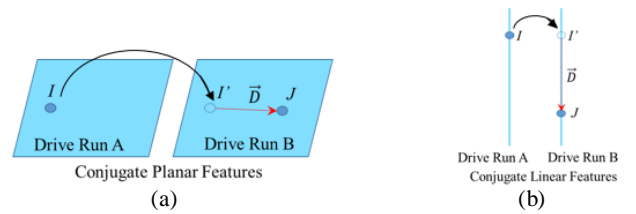


Figure 4. Discrepancy vector between non-conjugate points along corresponding (a) planar, and (b) linear features

$$P' \bar{D} = P' \begin{bmatrix} d_x \\ d_y \\ d_z \end{bmatrix} = 0 \quad (5)$$

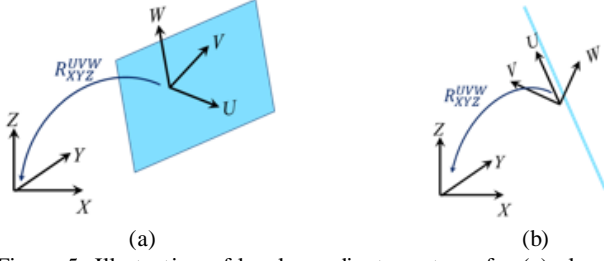


Figure 5. Illustration of local coordinate systems for (a) planar and (b) linear features

$$P_{UVW} = R_{XYZ}^{UVW} P_{XYZ} R_{XYZ}^{UVW T} = \begin{bmatrix} P_U & P_{UV} & P_{UW} \\ P_{VU} & P_V & P_{VW} \\ P_{WU} & P_{WV} & P_W \end{bmatrix} \quad (6)$$

$$\text{Linear/Cylindrical Feature: } P'_{UVW} = \begin{bmatrix} 0 & 0 & 0 \\ 0 & P_V & P_{VW} \\ 0 & P_{WV} & P_W \end{bmatrix} \quad (7)$$

$$\text{Planar Feature: } P'_{UVW} = \begin{bmatrix} 0 & 0 & 0 \\ 0 & 0 & 0 \\ 0 & 0 & P_W \end{bmatrix} \quad (8)$$

$$P'_{XYZ} = R_{XYZ}^{UVW T} P'_{UVW} R_{XYZ}^{UVW} \quad (9)$$

To achieve a higher precision in mounting parameters estimation from the calibration procedure, they need to be decoupled from each other. This decoupling can be achieved using multiple drive-runs. The discrepancies among conjugate features in such drive-runs are then used for estimating the mounting parameters. However, increasing the number of sensors and drive-runs would increase the complexity of extracting conjugate features. For instance, a patch, PI , extracted from different drive-runs (say, drive-run 1 and drive-run 2) and different sensors (say, sensor 1 and sensor 2) will lead to four separate versions for this feature. There will be six possible pairwise combinations for PI and the conditions to minimize the discrepancies within each of these pairs would no longer be independent. Hence, in this research, one of the versions is selected as reference to be paired with all the other versions of that feature from other sensors and/or drive-runs. The version with maximum number of points belonging to a feature is used as the reference version because this version will be used to derive the modified weight matrix for that feature. So, an increased number of points would increase the redundancy of plane or line/cylinder fitting for the feature, thus resulting in a more accurate estimate of the modified weight matrix. Finally, the mounting parameters for both reference and slave laser units can be derived by minimizing the discrepancies within the conjugate features arising from the above mentioned pairs between the different versions of such features.

However, when the initial estimate of mounting parameters is inaccurate, the estimated modified weight matrix would be imprecise which would affect the accuracy of the derived mounting parameters. Hence, this paper proposes an iterative calibration procedure. Firstly, the discrepancy among extracted features is minimized to derive mounting parameters through the weight modification process. Then, the points along the extracted features are re-generated using the new mounting parameters and the discrepancy among conjugate features is minimized again using a newly defined modified weight matrix. Then, the above steps are repeated until the change in the estimates of the mounting parameters is below a threshold.

4. EXPERIMENTAL RESULTS

4.1 Dataset Description

The data is captured by a designed platform which carries a VLP-16 and an HDL-32E laser scanner together with a SPAN-CPT direct geo-referencing unit, as shown in Figure 6. The five specially designed highly reflective boards are installed, oriented in different directions, in a sufficiently spacious area to drive around them. In this experiment, ten drive-runs, with different directions and lateral distance between them, were made around the five boards at an approximate speed of 4 miles/hr. With ten drive-runs and two laser units, we will have a total of 20 versions for each of the features used for the calibration procedure. The configuration of drive-runs and boards are shown in Figure 7. First, all the points are reconstructed using initial estimates of the mounting parameters, which are obtained from manual measurements/estimates for the lever-arm and boresight angles between SPAN-CPT and reference laser unit, and between the reference and slave laser units. The reconstructed point clouds are used to extract conjugate features. Then, the semi-automatic feature extraction is executed to obtain the points for planar features (i.e., specially designed boards and ground patches) from all the datasets separately, as shown in Figure 8. One should note that the modified weight matrix retains only the discrepancies in the direction normal to the planar surface. Therefore, the geometric direction of extracted features would be critical to conduct a successful calibration. In this experiment, the boards are set up to be perpendicular to each other. These boards, along with the extracted ground patches, ensure enough control along all the directions (i.e., X, Y, Z-directions). Three different test cases are considered for calibration: (1) single sensor calibration for VLP-16, (2) single sensor calibration for HDL-32E, and (3) multi-sensor calibration for VLP-16 and HDL-32E. The quality of the calibration results is then examined by performing a lane width evaluation using the calibrated mobile system consisting of both the VLP-16 and HDL-32E laser scanners.



Figure 6. Mobile Mapping System used in this research

The accuracy of calibration procedure is evaluated by monitoring the a-posteriori variance factor after every iteration of the least squares adjustment procedure and also, the RMSE of the normal distance of points belonging to a planar feature from the best-fitting plane for that feature.

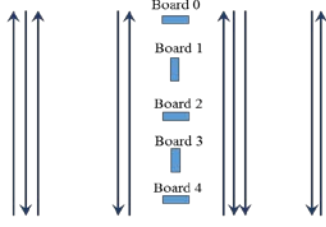


Figure 7. Configuration of drive-runs and calibration boards

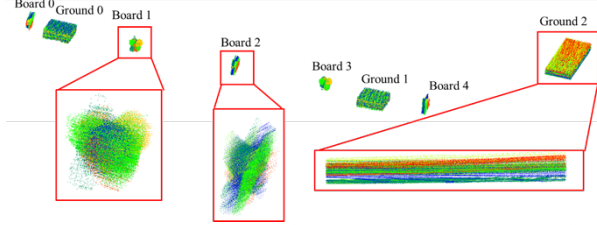


Figure 8. Features extracted from each version obtained from 2 different sensors and 10 different drive-runs (total of $2 \times 10 = 20$ different versions)

4.2 Dataset Description

A. Single Sensor Calibration Results

The mounting parameters that are derived in single sensor calibration are the planimetric lever arm components (ΔX , ΔY) and boresight angles ($\Delta \omega$, $\Delta \phi$, $\Delta \kappa$). The vertical lever arm component (ΔZ) is not adjusted in the calibration procedure. This is because any change in ΔZ will not introduce discrepancies among the different versions of the same feature captured from different sensors and/or runs. It would only result in a shift of the point cloud in the vertical direction as a whole. So, ΔZ is manually measured and fixed during the calibration procedure. The initial approximations of the mounting parameters and the final results from the single sensor calibration for VLP-16 as well as HDL-32E sensors are listed in Table 1.

Table 1. Mounting parameters of VLP-16 and HDL-32E before and after single sensor calibration

ΔX (m)	ΔY (m)	ΔZ (m)	$\Delta \omega$ (°)	$\Delta \phi$ (°)	$\Delta \kappa$ (°)
Initial Mounting Parameter					
VLP16 Mounting Parameters r_{VLP16}^b R_{VLP16}^b					
0.1	0.1	0.28	-10	0	-30
HDL32E Mounting Parameters r_{HDL32E}^b R_{HDL32E}^b					
0.4	0.1	0.3	-5	0	-60
Mounting Parameter After Calibration					
VLP16 Mounting Parameters r_{VLP16}^b R_{VLP16}^b					
0.006	0.189	0.28	-10.620	-1.006	-32.016
HDL32E Mounting Parameters r_{HDL32E}^b R_{HDL32E}^b					
0.475	0.195	0.3	-6.046	-0.064	-58.882

In single sensor calibration, the mounting parameters are derived based on conjugate planar features extracted from a single laser unit. For every iteration, the a-posteriori variance factor ($\hat{\sigma}_o$) of the least-squares adjustment procedure and the RMSE of normal distance of points from best-fitting plane for extracted features are derived to show the improvement. For single sensor calibration of the VLP-16 and HDL-32E scanners, the results are listed in Table 2 and Table 3, respectively.

Table 2. VLP-16 single sensor calibration: A-posteriori variance factor ($\hat{\sigma}_o$) and RMSE of plane fitting

	Number of Points	Before Calibration	Calibration Iteration 1	Calibration Iteration 2	Calibration Iteration 3
$\hat{\sigma}_o$ (m)			0.0470	0.0143	0.0143
Board 0 (m)	12,107	0.119	0.020	0.012	0.012
Board 1 (m)	13,787	0.148	0.143	0.013	0.013
Board 2 (m)	15,686	0.121	0.022	0.010	0.010
Board 3 (m)	13,015	0.130	0.142	0.011	0.011
Board 4 (m)	10,917	0.104	0.018	0.012	0.012
Ground 0 (m)	126,682	0.180	0.018	0.019	0.019
Ground 1 (m)	106,970	0.171	0.025	0.023	0.023
Ground 2 (m)	47,993	0.162	0.023	0.022	0.022

Table 3. HDL-32E single sensor calibration: A-posteriori variance factor ($\hat{\sigma}_o$) and RMSE of plane fitting

	Number of Points	Before Calibration	Calibration Iteration 1	Calibration Iteration 2	Calibration Iteration 3
$\hat{\sigma}_o$ (m)			0.0209	0.0138	0.0137
Board 0 (m)	50,222	0.128	0.019	0.019	0.019
Board 1 (m)	59,224	0.118	0.020	0.020	0.020
Board 2 (m)	70,216	0.125	0.016	0.016	0.016
Board 3 (m)	56,545	0.104	0.021	0.021	0.021
Board 4 (m)	44,469	0.112	0.014	0.014	0.014
Ground 0 (m)	554,942	0.154	0.022	0.021	0.021
Ground 1 (m)	502,867	0.146	0.021	0.020	0.020
Ground 2 (m)	137,191	0.178	0.024	0.023	0.023

It can be seen from the above tables that the RMSE for each feature is consistently improving after every iteration. In single sensor calibration, the accuracy can reach around 2 cm. One should note that the designed boards have a thickness of about 1 cm, so the RMSE will never be less than a centimeter. For VLP-16, the RMSE value is slightly smaller than HDL-32E. One of the possible reasons is that this research does not consider the sensor parameters. When the number of laser beams increases, the number of points would be more but the inconsistency would be more obvious for an object.

B. Multi-sensor Calibration Results

The mounting parameters that are derived in multi-sensor calibration are the planimetric lever arm components (ΔX , ΔY) and boresight angles ($\Delta \omega$, $\Delta \phi$, $\Delta \kappa$) for all the sensors and the vertical lever arm component (ΔZ) for all but the reference sensor. The ΔZ value for the reference sensor is not adjusted in the calibration procedure. This is because of the same reason as for the single sensor calibration. Fixing the value of ΔZ for the reference sensor would establish the datum for the data. So, it is manually measured and fixed during the calibration procedure. The initial approximations of the mounting parameters and the final results from the multi-sensor calibration for VLP-16 as well as HDL-32E sensors are listed in Table 4.

Table 4. Mounting parameters of VLP-16 and HDL-32E before and after multi-sensor calibration

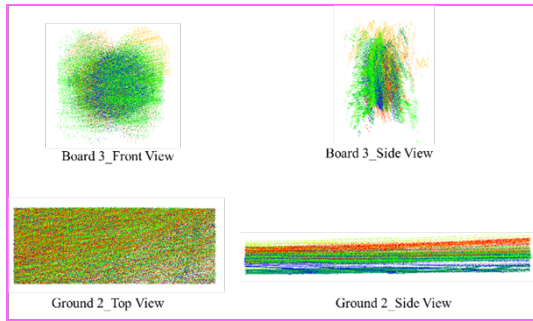
ΔX (m)	ΔY (m)	ΔZ (m)	$\Delta \omega$ (°)	$\Delta \phi$ (°)	$\Delta \kappa$ (°)
Initial Mounting Parameter					
HDL32E Mounting Parameters r_{HDL32E}^b R_{HDL32E}^b					
0.4	0.1	0.3	-5	0	-60
VLP16 Mounting Parameters r_{VLP16}^b R_{VLP16}^b					
-0.152	-0.259	-0.020	-2.505	-4.329	29.905
Mounting Parameter After Calibration					

HDL32E Mounting Parameters r_{HDL32E}^b R_{HDL32E}^b					
0.476	0.196	0.3	-6.045	-0.062	-58.881
VLP16 Mounting Parameters r_{VLP16}^{HDL32E} R_{VLP16}^{HDL32E}					
-0.247	-0.399	-0.078	-1.578	-4.327	26.839

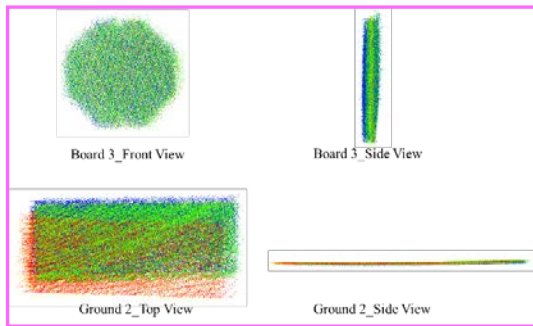
In multi-sensor calibration, the HDL-32E and VLP-16 scanners are taken as reference and slave units, respectively. The mounting parameters are derived simultaneously with point pairs from the conjugate features in the HDL-32E and VLP-16 datasets. For the multi-sensor calibration, the a-posteriori variance factor ($\hat{\sigma}_o$) of the least-squares adjustment procedure and the RMSE of normal distance of points from best-fitting plane for extracted features after every iteration are listed in Table 5. Through the qualitative evaluation depicted in Figure 9, one can observe a significant improvement of boards and ground patches after calibration. Moreover, a comparison is provided to assess the quality of single sensor calibration and multi-sensor calibration in Table 6.

Table 5. VLP-16 + HDL-32E multi-sensor calibration: A-posteriori variance factor ($\hat{\sigma}_o$) and RMSE of plane fitting

	Number of Points	Before Calibration	Calibration Iteration 1	Calibration Iteration 2	Calibration Iteration 3
$\hat{\sigma}_o$ (m)			0.0206	0.0134	0.0133
Board 0 (m)	62,329	0.127	0.018	0.018	0.018
Board 1 (m)	73,011	0.126	0.019	0.019	0.019
Board 2 (m)	85,902	0.124	0.015	0.015	0.015
Board 3 (m)	69,560	0.113	0.020	0.020	0.020
Board 4 (m)	55,386	0.114	0.014	0.014	0.014
Ground 0 (m)	681,624	0.164	0.022	0.022	0.022
Ground 1 (m)	609,837	0.156	0.021	0.021	0.021
Ground 2 (m)	185,184	0.212	0.025	0.024	0.024



(a)



(b)

Figure 9. Qualitative evaluation of some of the extracted boards and ground patches (a) before calibration, and (b) after calibration

Table 6. A comparison of single sensor calibration and multi-sensor calibration

	Number of Points	VLP-16+HDL-32E		VLP-16+HDL-32E	
		Before Single Sensor Calibration	After Single Sensor Calibration	Before Multi-Sensor Calibration	After Multi-Sensor Calibration
Board 0 (m)	62,329	0.126	0.018	0.126	0.018
Board 1 (m)	73,011	0.126	0.019	0.126	0.019
Board 2 (m)	85,902	0.124	0.015	0.124	0.015
Board 3 (m)	69,560	0.113	0.019	0.113	0.020
Board 4 (m)	55,386	0.114	0.014	0.114	0.014
Ground 0 (m)	681,624	0.160	0.032	0.160	0.022
Ground 1 (m)	609,837	0.151	0.031	0.151	0.021
Ground 2 (m)	185,184	0.196	0.031	0.196	0.024

From the comparison in Table 6, we can tell that the single-sensor calibration and multi-sensor calibration can reach similar accuracies for the board features but not for ground patches because in case of single-sensor calibration, the Z-value of lever arm will be fixed for both the sensors separately due to which the relative elevation between the two sensors will not be determined. But, in case of multi-sensor calibration, the Z-value of lever arm will be fixed only for one of the sensors which would lead to an accurate estimate for the relative elevation between the two sensors. Hence, the RMSE of ground patches after multi-sensor calibration are all smaller than the ones after single sensor calibration. Another benefit of multi-sensor calibration is that the mounting parameters for all the sensors can be derived simultaneously, but for single sensor calibration, each sensor has to be calibrated separately. So, the number of calibrations depends on the number of sensors.

C. Lane Width Evaluation

One of the applications of point cloud reconstruction is lane width evaluation for road safety inspection. When the lane width is narrow, it is considered less than the standard as it increases the probability of accidents and traffic congestions. So, after the calibration, the data collected for a road is reconstructed using the newly determined mounting parameters. Compared to asphalt, lane markers have higher reflectivity; hence, they can be identified from intensity data in a point cloud and used to determine the lane width. The point clouds from HDL-32E and VLP-16 with digitized lane markers (i.e., red and yellow dots) are shown in Figure 10. The normal distance from the red dots to yellow line (i.e., lane width) is shown in Figure 11. The ground truth of the corresponding area is shown in Figure 12. To evaluate the LiDAR-based lane width, the corresponding value from ground truth is computed by averaging four values, i.e., distance between inner bounds, outer bounds, inner and outer bounds, and outer and inner bounds of yellow and white line, respectively. The comparison of LiDAR-based lane width and its value from ground truth is shown in Figure 13.

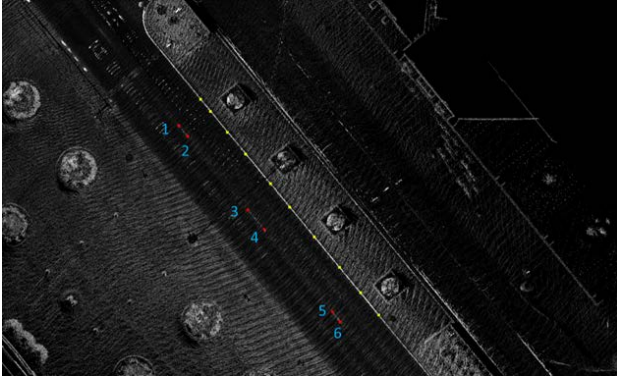


Figure 10. Digitized lane marker based on point clouds from HDL-32E and VLP-16, obtained from a single drive-run

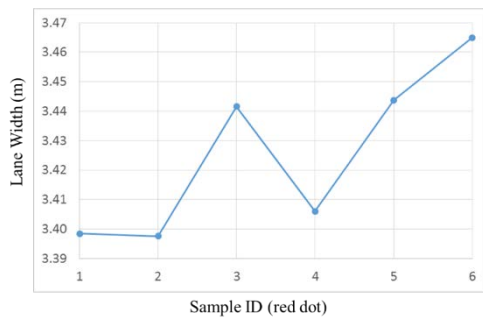


Figure 11. LiDAR-based Lane width obtained using the digitized points

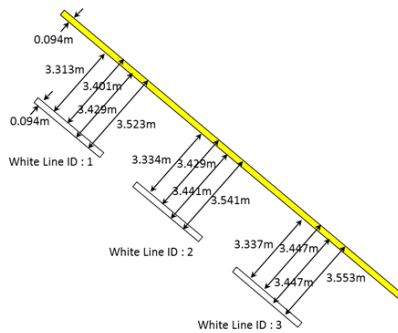


Figure 12. Ground Truth of Lane Width

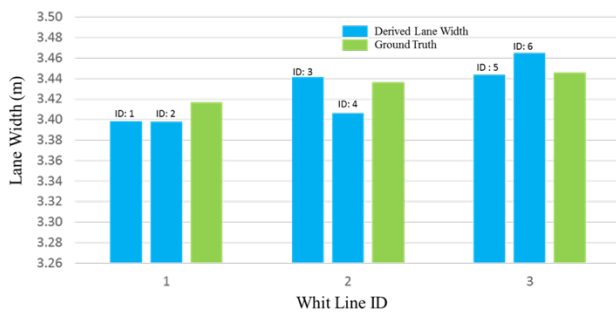


Figure 13. Comparison of LiDAR-based lane width and ground truth lane width

From Figure 13, it is inferred that the difference between the LiDAR-based lane width and ground truth ranges from 0.002 m to 0.030 m and the average is 0.015 m. Considering the random error in ground truth measurements, laser unit measurements, GNSS/INS measurements, and digitization of lane markers, an average bias of 0.015 m is acceptable for this application. From this experiment, it is demonstrated that the proposed calibration procedure can provide highly accurate mounting parameters and the generated point cloud can be used for applications with high accuracy requirements.

5. CONCLUSIONS AND RECOMMENDATIONS FOR FUTURE RESEARCH

In this paper, we provide a multi-sensor LiDAR system calibration method for deriving the mounting parameters simultaneously, instead of performing a separate calibration for each sensor. With the adopted modified weight matrix, the calibration procedure can utilize different types of conjugate features (i.e., planar, linear/cylindrical) at the same time. The proposed iterative calibration method is capable of deriving accurate mounting parameters, even if the initial estimates are considerably inaccurate. Both single unit calibration and multi-unit calibration are conducted using the proposed procedure and both of them can reach an RMSE value of 2 cm for the normal distances of the points from the best-fitting plane/line for the corresponding features. Moreover, this paper uses lane width evaluation to demonstrate that the proposed calibration procedure can derive the mounting parameters accurate enough to be used for an application with a high accuracy requirement. Future work will focus on combining the mounting parameters (i.e., extrinsic parameters) and sensor parameters (i.e., intrinsic parameters) to obtain a comprehensive calibration leading to even more accurate point clouds. Also, using lane markers as calibration primitives will also be investigated.

ACKNOWLEDGMENT

This work was supported in part by the Joint Transportation Research Program – administered by the Indiana Department of Transportation and Purdue University – and the Advanced Research Projects Agency-Energy (ARPA-E), U.S. Department of Energy, under Award Number DE-AR0000593. The implementation of the proposed methodology is supported by Ronald Benziger. The contents of this paper reflect the views of the authors, who are responsible for the facts and the accuracy of the data presented herein, and do not necessarily reflect the official views or policies of the sponsoring organizations.

REFERENCES

- Atanacio-Jiménez, G., González-Barbosa, J. J., Hurtado-Ramos, J. B., Ornelas-Rodríguez, F. J., Jiménez-Hernández, H., García-Ramírez, T., & González-Barbosa, R., 2011. LIDAR velodyne HDL-64E calibration using pattern planes. *International Journal of Advanced Robotic Systems*, 8(5), 59.
- Chan, T. O., Lichti, D. D., & Belton, D., 2013. Temporal analysis and automatic calibration of the velodyne HDL-32E LiDAR system. *ISPRS Annals of the photogrammetry, remote sensing and spatial information sciences*, 2(5/W2), 61-66.
- Choi, J., 2014. Hybrid map-based SLAM using a Velodyne laser scanner. In *Intelligent Transportation Systems (ITSC)*, 2014 IEEE 17th International Conference on (pp. 3082-3087). IEEE.

Glennie, C., Brooks, B., Ericksen, T., Hauser, D., Hudnut, K., Foster, J., & Avery, J., 2013. Compact multipurpose mobile laser scanning system—Initial tests and results. *Remote Sensing*, 5(2), 521-538.

Glennie, C. L., Kusari, A., & Facchin, A., 2016. Calibration and stability analysis of the vlp-16 laser scanner. *ISPRS-International Archives of the Photogrammetry, Remote Sensing and Spatial Information Sciences*, 3, W4.

He, M., Zhao, H., Davoine, F., Cui, J., & Zha, H., 2013. Pairwise LIDAR calibration using multi-type 3D geometric features in natural scene. In *Intelligent Robots and Systems (IROS)*, 2013 IEEE/RSJ International Conference on (pp. 1828-1835). IEEE.

Lin, H., Gao, J., Zhou, Y., Lu, G., Ye, M., Zhang, C., Liu, L. & Yang, R., 2013. Semantic decomposition and reconstruction of residential scenes from LiDAR data. *ACM Transactions on Graphics (TOG)*, 32(4), 66.

Novatel, 2014. Novatel SPAN-CPT User's Manual, <http://www.novatel.com/assets/Documents/Manuals/om-20000122.pdf> (Accessed 20 Feb 2017).

Puente, I., González-Jorge, H., Martínez-Sánchez, J., & Arias, P. (2013). Review of mobile mapping and surveying technologies. *Measurement*, 46(7), 2127-2145.

Schwarz, B., 2010. LIDAR: Mapping the world in 3D. *Nature Photonics*, 4(7), 429.

Underwood, J., Hill, A., & Scheduling, S., 2007. Calibration of range sensor pose on mobile platforms. In *Intelligent Robots and Systems*, 2007. IROS 2007. IEEE/RSJ International Conference on (pp. 3866-3871). IEEE.

Vallet, B., Xiao, W., & Brédif, M., 2015. Extracting mobile objects in images using a velodyne lidar point cloud. *ISPRS Annals of the Photogrammetry, Remote Sensing and Spatial Information Sciences*, 2(3), 247.

Velodyne, 2016a. Velodyne HDL-32E User Manual, http://velodynelidar.com/docs/manuals/63-9113%20REV%20K%20MANUAL,USER'S,HDL-32E_Outlined.pdf (Accessed 20 Feb 2017).

Velodyne, 2016b. Velodyne VLP-16 User Manual, <http://velodynelidar.com/docs/manuals/63-9243%20Rev%20B%20User%20Manual%20and%20Programming%20Guide,VLP-16.pdf> (Accessed 20 Feb 2017).

Williams, K., Olsen, M. J., Roe, G. V., & Glennie, C., 2013. Synthesis of transportation applications of mobile LiDAR. *Remote Sensing*, 5(9), 4652-4692.

Weiss, U., & Biber, P., 2011. Plant detection and mapping for agricultural robots using a 3D LIDAR sensor. *Robotics and autonomous systems*, 59(5), 265-273.